www.acsami.org



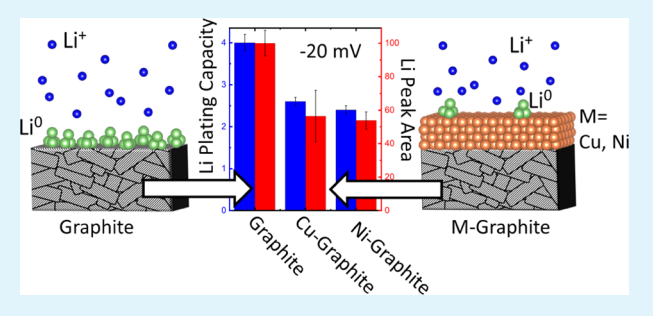


Anode Overpotential Control via Interfacial Modification: Inhibition of Lithium Plating on Graphite Anodes

Killian R. Tallman, Bingjie Zhang, Lei Wang, Shan Yan, Katherine Thompson, Xiao Tong, Juergen Thieme, Andrew Kiss, Amy C. Marschilok, Kenneth J. Takeuchi, David C. Bock, Sock, Kenneth J. Takeuchi, David C. Bock, Amy C. Marschilok, Kenneth J. Takeuchi, David C. Bock, Kenneth J. Takeuchi, Takeuch and Esther S. Takeuchi*,†,‡,§

Supporting Information

ABSTRACT: Lithium-metal deposition on graphite anodes limits the cycle life and negatively impacts safety of the current state of the art Li-ion batteries. Herein, deliberate interfacial modification of graphite electrodes via direct current (DC) magnetron sputtering of nanoscale layers of Cu and Ni is employed to increase the overpotential for Li deposition and suppress Li plating under high rate charge conditions. Due to their nanoscale, the deposited surface films have minimal impact (~0.16% decrease) on cell level theoretical energy density. Interfacial properties of the anodes are thoroughly characterized by atomic force microscopy (AFM), scanning electron



microscopy (SEM), X-ray photoelectron spectroscopy (XPS), and spatially resolved mapping X-ray absorption near edge structure (XANES) spectroscopy. The spectroscopic measurements indicate that the Cu and Ni coatings form oxide upon exposure to an ambient environment, but they are reduced within the electrochemical cell and remain in a metallic state. Li plating is quantified by X-ray diffraction and associated electrochemistry measurements revealing that the surface treatment effectively reduces the quantity of the plated Li metal by ~50% compared to untreated electrodes. These results establish an effective method using interfacial modification to achieve deliberate control of Li-metal deposition overpotential and reduction of lithium plating on graphite.

KEYWORDS: lithium plating, lithium-ion battery, fast charging, interfacial modification, graphite anode

1. INTRODUCTION

Lithium-ion battery technology is desirable for electric vehicles (EVs) due to the high voltage, small size, and light weight of lithium ion. In addition to high energy density, high power is required for vehicle technologies and fast charge capability is desired to facilitate consumer adoption. Notably, under fast charge conditions, lithium-metal deposition can occur at the graphite negative electrode. Without approaches to overcome this phenomenon, the rate at which lithium-ion cells can be charged is limited.³ Thus, renewed attention to interfacial phenomena at the negative electrode-electrolyte interface⁴ and particular attention to modification of graphite electrodes and characterization of their function under high current charge is merited and timely.

Plated Li metal can become isolated or react with the electrolyte consuming a portion of the cyclable lithium. This is a critical issue in Li-ion batteries where the lithium inventory is limited by the cathode, in contrast with Li-metal batteries where the lithium electrode affords an effectively unlimited supply. Physical isolation of the plated Li renders it electrochemically inactive and results in cell capacity loss.² During battery operation, graphite intercalation and Li deposition reactions can occur in parallel⁶

$$x \operatorname{Li}^+ + \operatorname{Li}_{\delta} C_6 + x e^- \to \operatorname{Li}_{(\delta + x)} C_6$$
 (1)

$$(1-x)\text{Li}^+ + (1-x)e^- \to (1-x)\text{Li}^0$$
 (2)

Equation 1 represents the graphite intercalation reaction, which occurs generally between 0.2 and 0.065 V vs Li/Li+, and eq 2 represents Li deposition. As previously derived, the condition for local Li deposition is met when the graphite electrode potential, E_{neg} , becomes less than or equal to the

Received: September 16, 2019 Accepted: November 22, 2019

Published: November 22, 2019



[†]Department of Chemistry and [‡]Department of Materials Science and Chemical Engineering, Stony Brook University, Stony Brook, New York 11794, United States

[§]Energy Sciences Directorate, "Science Undergraduate Laboratory Internship (SULI) Program, ¹Center for Functional Nanomaterials, and "National Synchrotron Light Source II, Brookhaven National Laboratory, Upton, New York 11973, United

 $^{^{}m V}$ Department of Chemistry and Physics, Mansfield University of Pennsylvania, Mansfield, Pennsylvania 16933, United States

potential $E_{\text{Li}^+/\text{Li}^0}$ in eq 3, including the contributions of overpotentials for both the graphite electrode (η_{neg}) and for the lithium deposition reaction $(\eta_{{
m Li}^+/{
m Li}^0})$

$$E_{\text{neg}} - \eta_{\text{neg}} \le E_{\text{Li}^+/\text{Li}^0} - \eta_{\text{Li}^+/\text{Li}^0}$$
 (3)

The three primary contributions to the overpotential for the graphite electrode (η_{neg}) in eq 3 are (1) electrode charge transfer, (2) mass transfer limitations in the electrolyte (concentration overpotential), and (3) lithium solid-state diffusion through graphite.⁷ The graphite overpotential is highly dependent on the charging conditions, where fast rates, low temperature, and high state of charge (SOC) all polarize the electrode and, thus, facilitate Li deposition.²

Prior strategies for suppressing Li plating on graphite have focused on minimizing η_{neg} , but only limited effectiveness has been demonstrated. Modifying the composition of the electrolyte, including the introduction of cosolvents or electrolyte additives, has been used to reduce charge transfer and concentration overpotential by reducing solid electrolyte interphase (SEI) resistance or increasing ionic conductivity.8 Additives that lower impedance of the negative electrode demonstrate the ability to decrease the onset current for Li plating, but only marginal improvement is observed vs the control electrolyte.8 Other approaches to increase lithium diffusion in the graphite anode have been accomplished by expansion of the graphite interlayer spacing, 10 the use of nanostructured carbon materials, 11 or etching graphite to increase its porosity. 12 However, associated disadvantages of these graphite modification strategies are that expanded graphite has reduced reversible capacity due to a lower degree of graphitization, ¹³ and increasing graphite surface area results in increased SEI formation and, thus, lower coulombic efficiency.2

In contrast to previous approaches for suppressing Li plating that focuses on decreasing the overpotential of the graphite electrode, herein we report an approach whereby the overpotential for Li-metal deposition $(\eta_{{
m Li}^+/{
m Li}^0})$ at the electrode surface is deliberately increased through a facile interfacial modification. Mathematical modeling 14,15 and experimental studies^{16,17} indicate that Li plating occurs primarily at the electrode surface, where the graphite overpotential is highest but can spread into the bulk of the electrode depending on the magnitude of overpotential as a function of electrode depth. During the deposition of Li via an electrocrystallization process, the free energy barrier for formation of Li nuclei must be overcome; however, the electrode surface-electrolyte interface can present additional resistance. An overpotential is needed to surmount the added energy cost and drive the reaction kinetics. In theory, the total overpotential for the electrocrystallization is the sum of four distinct contributions

$$\eta = \eta_{\rm ct} + \eta_{\rm d} + \eta_{\rm r} + \eta_{\rm c} \tag{4}$$

where $\eta_{\rm ct}$, $\eta_{\rm d}$, $\eta_{\rm r}$, and $\eta_{\rm c}$ are charge transfer, diffusion, reaction, and crystallization overpotentials, respectively.¹⁸ As shown in the recent work, 19 the electrode polarization during electrocrystallization of Li can be more simply described as the sum of two terms: the nucleation overpotential (η_n) , associated with initial nucleation of Li clusters and observed as an initial voltage drop, and the plateau overpotential (η_p) , which describes the continued growth of Li on existing nuclei. 20,21

The overpotential for Li electrocrystallization is highly dependent on the electrode substrate.^{22'} The driving force for the overpotential during Li nucleation is the interfacial energy difference between the substrate and Li metal, which is dependent on the dissimilarity in the crystal structure between Li and the substrate for deposition.^{22'} Specifically, Li metal crystallizes in the BCC form. 23 In this study, we demonstrate modification of the surface of the graphite electrodes with Cu or Ni metal, which both crystallize in an FCC structure. 24,25 Furthermore, neither Cu nor Ni forms an alloy phase with Li at room temperature and there is no single-phase solubility in Li at room temperature. 26 Thus, for heterogeneous nucleation to occur, an overpotential is necessary to overcome the energy barrier associated with the structural mismatch between Li and the Ni and Cu metal surfaces. ^{19,22} The deliberate increase in overpotential afforded by the metal coatings will impede the condition for Li nucleation (eq 4) from being reached, resulting in reduced nucleation sites on the metal-coated graphite surface. This is illustrated conceptually in Figure 1. It

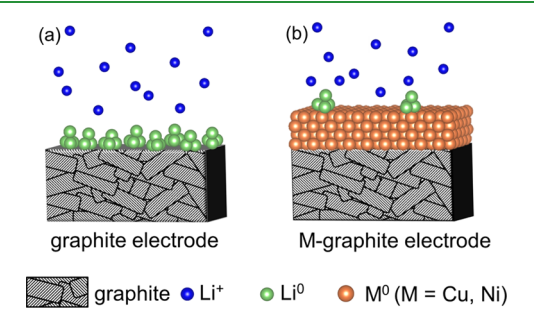


Figure 1. Schematic representation of (a) Li-metal nucleation on the graphite surface during high current charging and (b) reduced nucleation due to increased overpotential for Li-metal deposition afforded by a Cu or Ni surface coating with a structural mismatch.

should be noted that while the metal coatings will increase the overpotential for the initial nucleation of Li on the surface, they will not increase the overpotential for continued Li growth on existing nuclei. However, with fewer nucleation sites available for continued growth, the total quantity of Li plating is anticipated to be reduced in the presence of the metal-coated electrodes.

In the approach described herein, we use ultrathin (10 nm) metal coatings of Cu and Ni deposited on the surface of the graphite electrode. The metal coatings are characterized using scanning electron microscopy (SEM), atomic force microscopy (AFM), X-ray photoelectron spectroscopy (XPS), and X-ray absorption spectroscopy (XAS). We demonstrate that the approach reduces Li plating relative to untreated electrodes and improves the capacity retention of NMC622/graphite full pouch cells under extreme fast charging conditions. The results establish a transformative concept for reduction of Li plating on graphite via deliberate control of Li-metal deposition overpotential through surface modification.

2. EXPERIMENTAL SECTION

2.1. Electrode Preparation. Graphite electrodes were prepared by casting a slurry of 90 wt % natural graphite (SLC 1506T, Superior Graphite), 3 wt % conductive carbon black (Super P, Timcal), and 7 wt % poly(vinylidene fluoride) (PVDF; KF-9300, Kureha) in Nmethyl-2-pyrrolidone (NMP) onto a Cu foil (MTI). NMC622 cathodes were prepared using a slurry of 90 wt % NMC (Targray), 5 wt % conductive carbon black (Super P, Timcal), and 5 wt % poly(vinylidene fluoride) (Kynar) in NMP cast onto an Al-foil (MTI).

Direct current (DC) magnetron sputtering was performed using a Kurt J. Lesker 75 PVD sputtering instrument located at the Center for Functional Nanomaterials and Brookhaven National Laboratory. Cu and Ni sputtering targets were of 99.999% purity. Cu and Ni films (10 nm thick) were sputtered on as-prepared graphite electrodes using 100 and 200 W power for Cu and Ni, respectively, with a base pressure of 5 \times 10⁻⁶ Torr and working Ar pressure of 8 mTorr. Graphite electrode coatings with ~50 cm² area were sputtered at a time, and individual electrodes for coin cells or pouch cells were then cut from the sputtered electrode coatings. The deposition times necessary to produce 10 nm films were determined from calibration curves of deposited film thickness vs sputtering time.

2.2. Characterization of Metal Films. Scanning electron microscopy images with a backscatter detector were collected with an analytical high-resolution SEM (JEOL 7600F) instrument, operating at an accelerating voltage of 5 kV. Energy-dispersive X-ray spectroscopy (EDS) was collected using a JEOL JSM-6010PLUS instrument with an accelerating voltage of $20~\mbox{kV}$. AFM measurements were collected on a Park NX-20 in noncontact mode. Ultraflat SiO₂ wafers sputtered alongside the graphite anodes were used for the AFM analysis. Post-sputtering, a portion of the deposited coating was removed from the wafer by scratching with a pair of fine-tipped metal tweezers, creating a step between the metal-coated and uncoated areas. The process does not scratch the SiO₂ wafer itself; however, it can result in surface roughness in the crevice if the metal coating was not completely removed. Regions with minimized surface roughness were selected for AFM analysis.

XPS experiments were carried out in a UHV chamber equipped with a SPECS Phoibos 100 MCD analyzer. A nonmonochromatized Al K α ($h\nu$ = 1486.6 eV) X-ray source was used for the analysis of powders and electrodes. The accelerating voltage was 15 kV, and the current was 20 mA. The chamber had a base pressure of 2×10^{-9} Torr. Both powders and electrodes were pressed onto a conductive carbon tape and mounted on the sample holder. Charge correction for the data was done by adjusting the C 1s binding energy to 284.4 eV for graphitic carbon (sp²) or 285.0 eV for nongraphitic hydrocarbon (sp³) bonds.^{27–29} The XPS analysis regions measured were 925–970 eV for Cu 2p, 560-590 eV for Cu LMM, 845-890 eV for Ni 2p, 280-295 eV for C 1s, 525-540 eV for O 1s, 680-695 eV for F 1s, and 50-60 eV for Li 1s. Epass of 25, step size of 0.05 eV, and scan number of 10 were applied to measure each individual region. Selected Cu-graphite and Ni-graphite electrodes, which had undergone formation cycling, were Ar-sputtered for 0.5 h before XPS measurements to obtain an adequate signal from Cu and Ni. Ar sputtering was performed at room temperature with a pressure of 2 × 10⁻⁵ Torr using an energy of 2 keV.

X-ray microfluorescence (*µ*-XRF) mapping and X-ray absorption spectroscopy (XAS) measurements of Li/graphite experimental cells were acquired at beamline 5-ID of the National Synchrotron Light Source II (NSLS-II) at Brookhaven National Laboratory. Data acquisition and visualization were performed using the python-based beamline software developed for NSLS-II Beamline 5-ID. µ-XRF maps were generated by fitting the fluorescence spectra using PyXRF python-based X-ray fluorescence analysis package.³⁰ XAS data were aligned and normalized using the Athena software.³¹ Operando X-ray absorption near edge structure (XANES) measurements were performed in custom-built pouch type electrochemical cells with either Cu-graphite or Ni-graphite working electrodes and Li counter electrodes. Operando cells were (dis)charged at the C/5 rate between 0.01 and 1.3 V. Linear combination fitting (LCF) of the X-ray absorption near edge structure (XANES) was performed using the Athena software.³¹ LCF fits were performed on data 20 eV below to 20 eV above the edge energy (E_0) .

2.3. Electrochemical Measurements. Graphite, Cu-graphite, and Ni-graphite electrodes were used in the assembly of half cells in a coin cell format with Li counter electrode, polypropylene separator, and 1 M LiPF₆ 30:70 EC/DMC electrolyte. Electrode diameter for coin cells was 7/16". A cell formation protocol of four cycles at the C/ 10 rate between 0.01 and 1.3 V was used prior to electrochemical impedance spectroscopy (EIS) measurements and C/2 cycling. PEIS

measurements were collected using a Bio-Logic VSP potentiostat between 1 MHz and 10 mHz with a 5 mV sinus amplitude. For Li plating experiments, the electrodes underwent one formation cycle at the C/10 rate and a second discharge at C/10 to 0 V prior to being subjected to voltage holds of -10, -15, or -20 mV for 6 h. Postelectrochemical testing, coin cells were disassembled under an inert atmosphere. Disassembled graphite electrodes were rinsed with a dimethyl carbonate solvent and dried under vacuum. The electrodes were kept under an inert atmosphere for X-ray diffraction (XRD) measurements by employing a sample holder with a beryllium window and an O-ring seal. XRD measurements were recorded with a Rigaku SmartLab X-ray diffractometer, using Cu Klpha radiation and Bragg-Brentano focusing geometry. Scanning electron microscopy (SEM) analyses of the Li-plated electrodes were conducted using a IEOL 7600F instrument.

Full cell experiments were performed in single-layer pouch cells with graphite electrodes paired with NMC622 cathodes. The negative to the positive capacity ratio in the cells was 1.15 with electrode sizes of 23.7 and 20 cm² for the anode and cathode, respectively. Areal loadings of the anode and cathode were 8.3 and 16.4 mg/cm², and their porosities were 43 and 35%, respectively. The cells were prepared with a polypropylene separator and 1 M LiPF₆ 30:70 EC/ DMC electrolyte. A cell formation protocol of four cycles at the C/10 rate between 3.0 and 4.3 V was used to condition the cells prior to additional cycling. Cells were cycled under two protocols: (1) C/2 discharge and charge between 3.0 and 4.3 V and (2) 1C discharge and a charge time limited to 10 min using a 6C constant current step to 4.3 V followed by a constant voltage step at 4.3 V for the remainder of the 10 min segment. Two cells per group (graphite, Ni-graphite, Cu-graphite) were used to assess the reproducibility of the data.

3. RESULTS AND DISCUSSION

3.1. Surface Modification of Graphite with Nanoscale Cu and Ni Layers. Metal-coated graphite electrodes were prepared using DC magnetron sputtering to deposit 10 nm films of Cu or Ni. Based on previous reports that provided proof of concept for Li intercalation through 5-40 nm thick films of Cu^{32–35} and 7.5 nm films of Ni, ³⁶ 10 nm was selected as the initial thickness for our study. At this thickness, the contributions of the metal coatings to the inactive mass of the electrode are insignificant: for a 1 Ah NMC622/graphite pouch cell with total 320 cm² electrode area, 20 mg/cm² cathode loading, and negative to positive capacity ratio of 1.15, the extra mass contributed by the metal coatings on the anode would result in only a 0.16% decrease in energy density (Table S1). Thus, the technical approach maintains cell-specific energy relative to the current state of the art batteries. It is noted that while in this study a PVDF-based binder was used to fabricate the anodes, the metal coatings are anticipated to be transferrable to aqueous-based binder systems such as carboxymethyl cellulose (CMC)/styrene butadiene rubber (SBR) binder that is used in state of the art anodes.³⁷ The metal coatings are applied to the anodes after the anodes have been fabricated and solvent has been evaporated. Thus, the protic media used to process the CMC/SBR binder system will never be in contact with the surface metal films and, therefore, will not alter the oxidation state of the metals.

The prepared samples were characterized using scanning electron microscopy (backscatter imaging mode, BSE, Figure 2). The BSE yield dependence on Z enables clear contrast between pristine graphite and graphite coated with the metal films. Images of the electrodes collected from the top-down indicate that the upper surfaces of the electrodes have a uniform coating with Cu or Ni (Figure 2a,f). SEM-BSE images of the electrode cross-sections (Figure 2g,i) reveal that the sputtered films are predominant at the electrode surface.

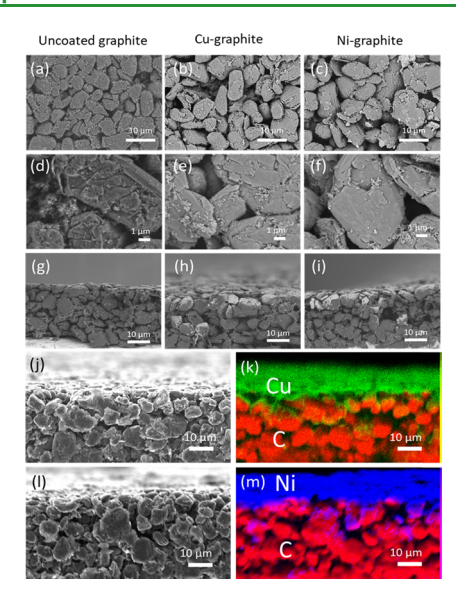


Figure 2. (a-i) SEM backscatter images of graphite electrodes (a, d, g) pristine, (b, e, h) sputter-coated with 10 nm Cu, and (c, f, i) sputter-coated with 10 nm of Ni. Images (a)-(i) show the samples measured top-down, while (i)-(m) show cross-sectional images of the electrodes. Small (~20-100 nm) particles observed in the electrodes are carbon black conductive additive. (j, l) SEM secondary electron images and (k, m) corresponding composite EDS maps for graphite electrodes sputtered with (j, k) 10 nm Cu and (l, m) 10 nm Ni, respectively. For EDS maps, red, green, and blue pixels correspond to X-ray signals from C, Cu, and Ni, respectively.

Energy-dispersive spectroscopy (EDS) mapping was used to further characterize the films (Figure 2k,m; Figure S3). EDS maps of the electrode cross-sections (Figure 2k,m) definitively show that the deposited Cu and Ni are located on the upper surface of the graphite anode. EDS maps collected from the top-down (Figure S3) show that the deposited films are relatively uniform on the graphite particles on the electrode surface. Changes in surface roughness imparted from the metal coatings are negligible. The height variation in the uncoated graphite electrode surface is on the order of 1–10 μ m, due to crevices between adjacent micron-scale graphite particles that comprise the electrode, which is approximately 2-3 orders of magnitude greater than the thickness of the metal coatings (10 nm).

While the SEM images indicate that the metal films are limited to the upper surface of the graphite electrode, in a charging Li-ion battery, Li deposition occurs mainly at the electrode-separator interface. Mathematical models predict that Li plating occurs primarily at the graphite surface, due to the high graphite electrode overpotential in this region. 14,15 Experimentally, glow-discharge optical emission spectroscopy depth profiling (GD-OES) experiments show that most plated Li occurs at the anode/separator interface, but that the deposited Li also spreads into the bulk of the electrode by approximately 10 μ m. ^{16,17} The extent to which Li deposition occurs in the electrode bulk is dependent on the magnitude of the overpotential as a function of electrode depth. 14,115

The thicknesses of the deposited Cu and Ni films were verified via atomic force microscopy (AFM) of ultraflat SiO₂ wafers sputtered alongside the graphite anodes. Representative AFM images for the analyzed SiO₂ wafers are shown in Figures S4 and S5. The average Cu and Ni thicknesses determined from this method were 10.2 ± 0.6 nm (n = 10) and 9.7 ± 0.7

nm (n = 10), respectively, indicating consistent preparation under controlled experimental conditions.

3.2. X-ray Photoelectron Spectroscopy Character**ization.** The surface composition and oxidation state of the asprepared Cu and Ni films on graphite electrodes, as well as the coated electrodes after undergoing formation cycling, were probed using X-ray photoelectron spectroscopy (XPS) (Figure 3, Table S2). The Cu 2p_{3/2} spectrum of the as-prepared Cu-

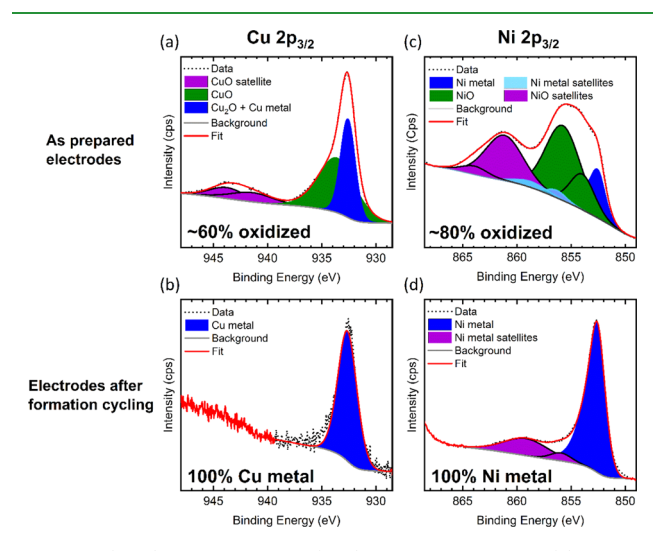


Figure 3. (a-d) XPS spectra of (a, b) Cu 2p_{3/2} region of (a) pristine 10 nm Cu-graphite electrode and (b) 10 nm Cu-graphite electrode after formation cycling (charged state) and Ar sputtering; (c, d) Ni 2p_{3/2} region of (c) pristine 10 nm Ni-graphite electrode and (d) 10 nm Ni-graphite electrode after formation cycling (charged state) and Ar sputtering.

coated graphite electrode shows a contribution from CuO, including the main peak at ~933.6 eV as well as two satellite peaks around 942 eV, in good agreement with the literature (Figure 3a). 38,39 Additionally, there is another peak at ~ 932.6 eV, which corresponds to Cu metal and Cu₂O species in the sample. Since Cu metal and Cu₂O species have overlapping binding energies and cannot be deconvoluted, the peak is fit to both Cu₂O and Cu species. Based on the fitting results and calculation reported in the literature, ³⁸ ~60% of Cu on the surface is oxidized. In fact, the Cu LMM spectra, shown in Figure S6, indicate Cu₂O as the dominant species on the surface.

XPS analysis of the pristine Ni-coated graphite electrode indicates that the surface is comprised of NiO and Ni metal (Figure 3c). Two main peaks positioned at \sim 855.8 and \sim 854.0 eV correspond to NiO, while a peak at ~852.6 eV relates to Ni metal (Table S1). These fitted main peaks and the satellite peaks are in good agreement with previous reports of NiO and Ni metal phases. 40,41 Analysis of the relative peak areas yielded the percent composition to be \sim 80% NiO on the surface of the as-prepared electrode. Both metal films exhibit significantly oxidized surfaces indicating that substantial air oxidation of the deposited metal occurred, likely as a result of storing the samples in the ambient atmosphere.

Analysis of the metal-coated electrodes after undergoing formation cycling (ending in the delithiated state) was performed to elucidate how the oxidation state of the films evolved after electrochemical cycling. Ar sputtering had to be performed on the electrodes to observe the signal from Cu and

ACS Applied Materials & Interfaces

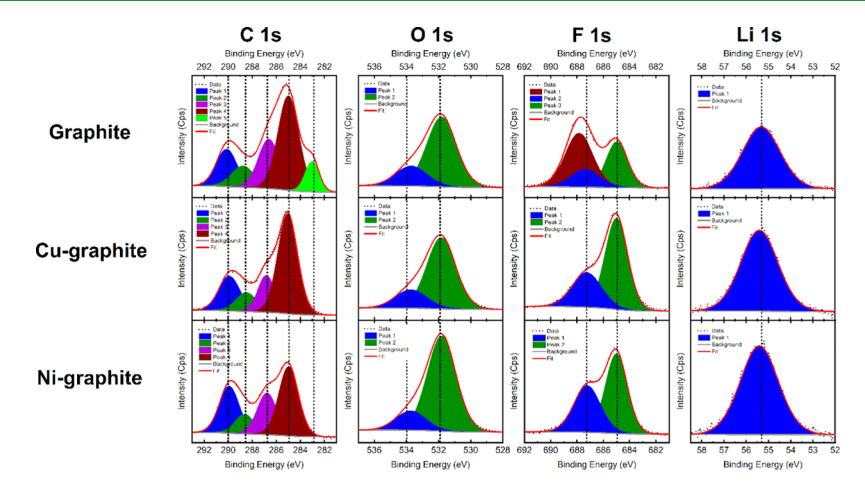


Figure 4. XPS C 1s, O 1s, F 1s, and Li 1s spectra for uncoated graphite (control), Cu-graphite, or Ni-graphite anodes after formation cycling. No Ar sputtering was performed on these samples. Plots of each respective spectral region are shown on the same scale.

Ni transitions (Figures S7 and 3), likely due to SEI formation on top of the metals that dampened the signal from the metal photoelectrons. Ar sputtering experiments performed on pristine metal-coated electrodes were used to verify that the Ar sputtering process did not artificially reduce the films (Figure S9). After formation cycling, the Cu film consists of a single peak at ~932.6 eV, with the peak corresponding to CuO species no longer observed. While contributions of Cu₂O and Cu metal species cannot be deconvoluted from the Cu 2p spectra, X-ray-generated Cu LMM spectra can be used to distinguish Cu₂O from the Cu metal.³⁸ Comparison of LMM spectra for Cu standards to the Cu-graphite electrode after formation (Figure S6) indicates that that Cu₂O is not present. Thus, the combination of the Cu 2p and Cu LMM spectra exhibits Cu metal as the primary species.

The assignment of the Ni 2p_{3/2} spectrum of a Ni-coated graphite electrode after undergoing formation cycling is well fit to Ni metal. The main Ni metal peak at ~852.6 eV and two satellite peaks are good agreement with the literature. 40,41 Thus, both Cu- and Ni-deposited films are oxidized but electrochemically reduced to Cu and Ni metal during formation. For a 1 Ah NMC622/graphite pouch cell with total 320 cm² anode area, 10 mg/cm² anode loading, and negative to positive capacity ratio of 1.15, the electrochemical reduction of the metal oxide films would consume 0.13 and 0.15% of the total lithium inventory in the cell (Table S1). The loss of this quantity of Li would not significantly affect the N/P capacity ratio of the cell.

The electrochemical reduction of the oxides during the lithiation reaction is also anticipated to form Li₂O as an additional reaction product. 42,43 The formed Li₂O is not expected to have a significant impact on the electrochemical performance because (1) Li₂O is already a major component of the SEI formed on graphite anodes⁴⁴ and (2) it has a similar Li-ion diffusion coefficient compared with LiF and Li₂CO₃, two other primary inorganic components of the SEI.⁴⁵

The XPS data indicates that the Cu and Ni films are not reoxidized during the delithiation (oxidation) process and remain in the metallic state. In apparent contrast to this result, previous literature demonstrates that CuO and NiO are able to reversibly store Li ions by reducing to Cu and Ni metal (and ${\rm Li_2O})$ during lithiation and by reoxidizing back to their pristine state during delithiation. 42,46–48 However, cyclic voltammetry experiments indicate that the reoxidation reaction occurs at approximately 2.45 V vs Li/Li⁺ for CuO electrodes^{42,48} and 2.25 V vs Li/Li⁺ for NiO electrodes. 46,47 In comparison, the metal coatings on graphite electrodes investigated herein are delithiated to a voltage of only 1.3 V vs Li/Li⁺ due to the limited (de)intercalation voltage window for graphite. The 1.3 V maximum is far below the required voltage for reoxidation of the metals. Furthermore, in a practical Li-ion cell with an appropriate cell anode:cathode capacity ratio, the voltage of the graphite electrode will not increase beyond 1.3 V vs Li/Li⁺ during battery discharge, thus the coatings will remain in the metallic state.

The chemistry of the solid electrolyte interphase layer formed on the electrodes was also investigated using X-ray photoelectron spectroscopy. SEI is known to form on graphite electrodes and functions as an ionically conductive and electronically resistive solid electrolyte. 49' Li-metal electrodeposition occurs underneath the solid electrolyte interphase, directly on the electrode, rather than on top of the SEI. Continued lithium growth can pierce through the SEI film and contact the SEI, resulting in additional film formation; however, Li does not plate on top of the SEI because the SEI is electrically insulating. 51,52 XPS C 1s, O 1s, F 1s, and Li 1s spectra of formation cycled electrodes (ending in the lithiated state) are presented in Figure 4 and Table S3. A full description of the results is presented in the SI. Four C 1s peaks are found at ~290.0, ~288.6, ~286.7, and ~285.0, which correspond to carbonate, carboxylate, ether, and hydrocarbon groups, for each sample with similar quantities. However, an additional peak at ~283 eV appears in the uncoated lithiated electrode C 1s spectra corresponding to Li-C. This peak is commonly observed in SEI studies of graphite and is attributed in the literature to either lithiated graphite species $\text{Li}_{r}\text{C}_{6}^{53,54}$ or lithium carbide. 29,55 This peak exhibits the only major difference between samples for the C 1s, O 1s, and Li 1s spectra, indicating similar SEI chemistry in the presence of the metal coatings. No signal from Cu or Ni transitions was observed without Ar sputtering (Figure S7), which strongly suggests that the SEI is formed on top of the surface metal film and its thickness is sufficient to dampen the metal photoelectron signals.

The Li–C peak is detected for the control graphite electrode but not for the metal-coated electrodes. We hypothesize that the peak arises primarily from Li_xC_6 species, $^{53, \cancel{54}}$ and that it is only observed in the control graphite electrode because of the

ACS Applied Materials & Interfaces

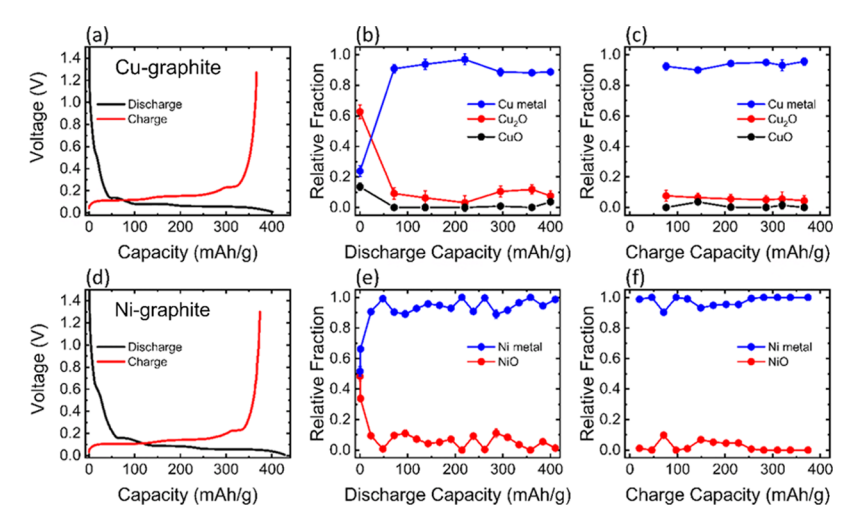


Figure 5. Operando XANES results for (a-c) Cu-graphite electrodes and (d-f) Ni-graphite electrodes during a formation cycle at the C/5 rate between 0.01 and 1.3 V vs Li/Li⁺. (a, d) Voltage profiles of operando cells. (b, c, e, f) Linear combination fit results for operando spectra during (b, e) discharge and (c, f) charge.

effect that the metal film and SEI layers have on the XPS sampling depth. This observation is rationalized by the inability of the Li-C photoelectrons to reach the surface of the sample due to the thickness of the metal film as well as the SEI layer. Based on the inelastic mean free path, the escape depth of 95% of the photoelectrons is calculated to be ~9 which is less than the combination of the 10 nm metal film and the SEI layer. This rationale is further supported by the as-prepared uncoated and metal-coated XPS results of the C 1s, F 1s, and O 1s spectra shown in Figure S8 and tabulated values in Table S4. The intensity of the C 1s peak decreased by a factor of ~5 when comparing the uncoated electrode to the metal-coated electrodes due to the impact of the metal films on the detection of graphitic photoelectrons from the underlying graphite. Furthermore, the F 1s peak signal is significantly dampened by the metal coating and is only weakly distinguishable from the background. This difference can be quantified to a factor of ~20 because of the lower sampling depth of the lower kinetic energy F 1s photoelectrons, ~7 nm. 54,5

The F 1s spectra of the cycled electrodes also show significant differences between the uncoated and metal-coated electrodes. The two observed peaks for the metal-coated samples are located at ~687.3 and ~685.0 eV, which correspond to P-F from electrolyte salt degradation products (denoted as $\text{LiP}_x F_v$) and Li-F, respectively. 29,54,59-61 For the uncoated electrode, the higher binding energy peak significantly shifts to higher energy, indicating that another species is contributing to the signal. The fitted spectrum matches the two peaks for P-F and Li-F but has an additional peak at ~687.8 eV that corresponds to C-F groups in the PVDF binder. PVDF peaks have been previously reported at binding energies close to ~688 eV. 29,62,63 This finding is in good agreement with the pristine graphite electrode fitting results reported herein (Figure S8), which clearly indicate a peak at ~687.8 eV attributed to PVDF. As mentioned previously, the absence of a metal film to dampen the F 1s signal in the uncoated electrode allows the binder component to contribute to the signal.

Based on the XPS results, the chemistry of the SEI film is not significantly affected by the deposited Cu or Ni and is not anticipated to have a large impact on the electrochemical behavior. Furthermore, because spectra associated with SEI

components are detected on the metal-coated electrodes even though the analysis depth of the measurement is less than the thickness of the metal coatings, the data suggests that significant SEI formation occurs on the upper surface of the deposited metal layers.

3.3. Operando XANES Characterization. Operando Xray absorption near edge structure (XANES) spectroscopy measurements collected on the electrodes during the initial formation cycle to probe the changes in the oxidation state of the films with discharge and charge (Figures 5 and S10). Operando XANES measurements of relevant standards for Cu (Cu₂O powder, CuO powder, Cu metal foil) and Ni (NiO powder, Ni metal foil) were collected, and linear combination fitting (LCF) was performed to estimate the phase compositions of the deposited metal films as a function of (de)lithiation. LCF results show that the as-prepared 10 nm Cu-coated graphite electrode is a mixture of ~22% Cu metal, ~61% Cu₂O, and ~17% CuO. Notably, the results demonstrate that during formation cycling, the Cu oxides that comprise the film are fully reduced to Cu metal during the initial lithiation and do not reoxidize during delithiation, in good agreement with the XPS results. Similarly, the 10 nm Ni-graphite coating in the as-prepared state exhibits a composition from LCF fitting of ~50% NiO and ~50 Ni metal. The film is irreversibly reduced to 100% Ni metal during the formation cycle and does not reoxidize on charge within the voltage window used. It is notable that while there is excellent oxidation state agreement between XANES and XPS results for the films after formation cycling, the XANES analyses of the as-prepared Cu-graphite and Ni-graphite electrodes indicate that the films are less oxidized when compared to the XPS results. We rationalize this finding by comparing the differing analysis depths for the two techniques: for XPS, based on the inelastic mean free path of electrons in Cu and Ni, the analysis depth is estimated to be less than \sim 5 nm, while the XANES measurements are representative of the entire 10 nm thick films.

X-ray fluorescence elemental mapping was used to further probe the uniformity of the Cu and Ni films on the graphite anode before and after formation cycling (Figure S11). XRF maps suggest that the Cu and Ni films show some compositional variation on the surface of the electrodes, as **ACS Applied Materials & Interfaces**

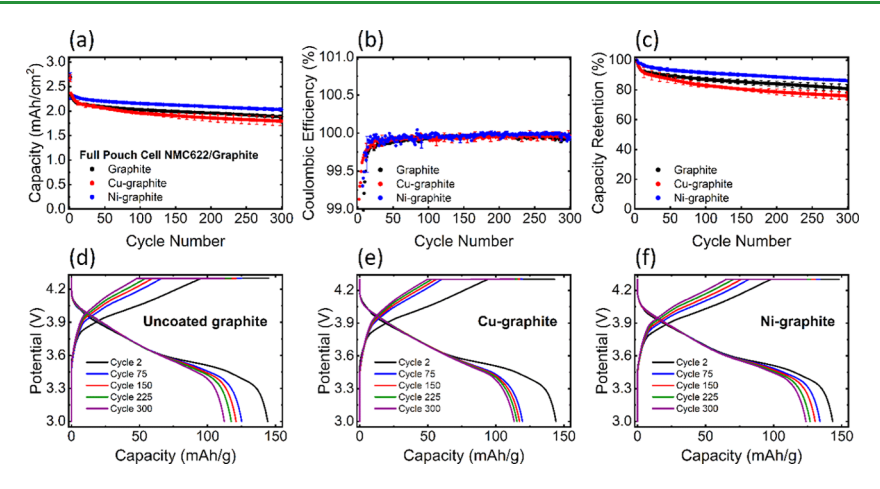


Figure 6. Cycling of graphite/NMC622 cells under 1C discharge and a total charge time of 10 min, with a 6C constant current step followed by a constant voltage step at 4.3 V for the remainder of the 10 min. (a) Areal capacities, (b) coulombic efficiency, and (c) capacity retention. Error bars shown in the plots are representative of one standard deviation from the mean (n = 2). (d-f) Representative voltage profiles for (d) pristine graphite electrodes, (e) graphite electrodes sputtered with 10 nm Cu, and (f) graphite electrodes sputtered with 10 nm of Ni. Error bars represent one standard deviation from the mean (n = 2). Capacity retention is calculated relative to cycle 2 discharge capacity, the first cycle under the fast charge condition.

evidenced by fluorescence counts, which vary between 50 000 and 150 000. This variation is believed to be due to the intrinsic height variability of the electrode surface, which is on the scale of several microns since the dimeter of graphite particles in the electrode is $\sim 10 \mu m$. After formation cycling, similar variation in fluorescence intensity is observed, confirming that the metal films are not disrupted by the (de)lithiation process.

3.4. Electrochemical Characterization. The galvanostatic voltage profiles of the metal-coated electrodes compared to control graphite electrodes were probed in a half cell configuration. C/10 voltage profiles are shown in Figure S12, and tabulated capacities are presented in Table S5. Under this test condition, the voltage profiles show no significant differences between groups, and the metal coatings do not increase polarization during (de)lithiation. Furthermore, the results confirm that reduction of the metal films does not significantly contribute to the irreversible capacity during initial cycling.

Impedance response of the metal-coated electrodes was also characterized in half cells post-formation cycling (Figure S13, Table S6). The collected impedance spectra were fit to an equivalent circuit model that is a modified version of the Randles circuit, 64 with RC elements in series. The first resistor, R₁, represents DC electrolyte resistance as well as ohmic resistances of the cell components. R2 and CPE1 in the first RC element and R3 and CPE2 in the second RC element are used to fit the high to medium semicircular features in the Nyquist plot and correspond to the ionic resistance and capacitance of the surface films on the Li metal and graphite electrodes in the cell. The fourth resistor (R₄) and Warburg element in parallel with the constant phase element (CPE3) are used to fit the middle to low-frequency range spectra and approximate the charge-transfer resistance, double-layer capacitance, and diffusion coefficient of Li+ in the graphite electrode. The EIS fitting results indicate that the metal coatings have little to no effect on the ionic resistance of the electrode. Previous reports have demonstrated that Li⁺ ions can effectively (de)intercalate through nanometer-scale films of both Cu^{32-35,65} and Ni, 36,66 supporting the current results.

The functional capacity of the metal-coated anodes compared to pristine graphite anodes was investigated in a single-layer pouch cell configuration with paired NMC622 cathodes. Bar graphs showing the statistical differences between the capacity retention for the C/2 cell data and 6C/1C data are presented in Figure S14 and show a significantly higher fade at the 6C charge rate. Under the C/ 2 rate, average first cycle areal capacity, capacity retention, and coulombic efficiency over 300 cycles were within error for the three groups (Figure S15). However, when charging time is reduced to 10 min (Figure 6), differences are observed between the electrode types. While the first cycle capacities are within error, by cycle 75, the cells containing the Ni-graphite electrodes exhibit improved capacity retention compared to the pristine graphite and Cu-graphite electrodes. The result suggests that the Ni-coating hinders Li deposition under extreme fast charging conditions. The ~5% improvement in capacity retention afforded by the Ni-graphite electrode represents a significant improvement in performance for technologically matured Li-ion technology.

Electrodes were harvested from cycled cells in the charged state for each C/2 and 6C/1C condition to visually evaluate any changes to the electrodes as a result of the cycling rate. Images of the graphite, Cu-graphite, and Ni-graphite anodes post-cycling are displayed in Figure S16. The cell design, configuration, and electrode balance seem appropriate based on the lack of any significant feature changes to the anodes after 300 cycles at a C/2 rate. However, in the case of 6C/1C cycling, there is clear evidence of Li plating by the white/silver color on the surfaces of each of the six electrodes. Intriguingly, the plated Li distribution on the anodes varies. When considering these cells individually or as duplicate cell groups, it is apparent that both Ni-graphite anodes present noticeably less plated Li than the control uncoated graphite anodes. The Cu-graphite anodes appear to also reveal slightly less Li plating compared to the control; however, they are too similar to form a conclusion solely based on inspection. It is notable that the amount of plated Li on the cycled anodes correlates very well with the cycling results during extreme fast charging conditions. The Ni-graphite shows the best performance and the lowest quantity of plated Li while there are no significant

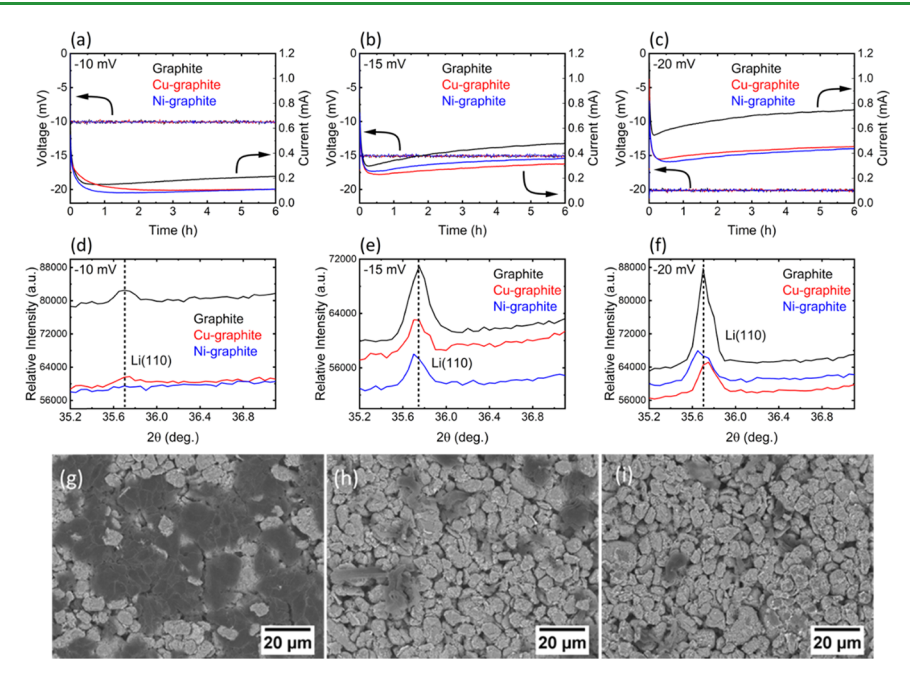


Figure 7. Plots of current and voltage vs time for graphite, Cu-graphite, and Ni-graphite held at (a) -10 mV, (b) -15 mV, and (c) -20 mV for 6 h. (d-f) Corresponding X-ray diffraction patterns of electrodes after Li plating showing Li-metal (110) peak. (g-i) LABE SEM images displaying the morphologies of Li plated at -20 mV on the (g) uncoated graphite, (h) Cu-coated graphite, and (i) Ni-coated graphite electrodes.

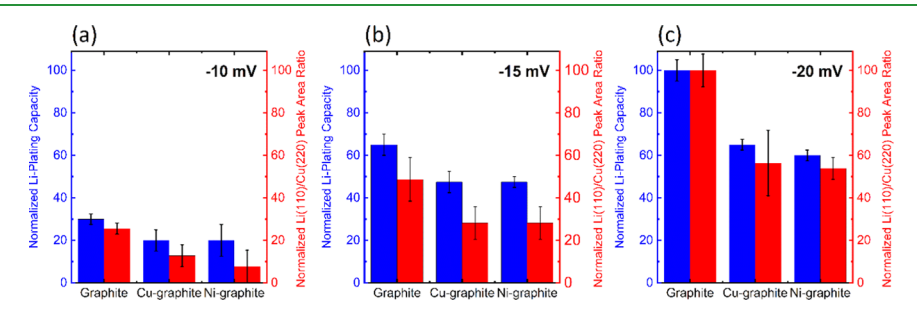


Figure 8. Normalized Li-plating capacities and normalized Li(110)/Cu(220) peak area ratios from XRD measurements for fully lithiated electrodes subjected to voltage holds of (a) -10, (b) -15, and (c) -20 mV for 6 h.

differences between the plated Li amount and cycling performance of the graphite and Cu-graphite cases. While it is unclear why Cu does not behave similarly to Ni, we hypothesize that Li⁺ diffusion rate through the deposited metal films may not be equivalent for Ni and Cu. Studies of the effects of metal coating thickness on Li plating in full cell configuration are underway to test the hypothesis.

Lithium plating experiments were performed to evaluate the effectiveness of the Cu and Ni films at reducing Li-metal deposition compared to uncoated graphite. Li-metal half cells with fully lithiated electrodes were subjected to voltage holds of -10, -15, and -20 mV for 6 h (Figure 7a,c). Under these electrochemical conditions, where the voltage of the graphite electrode is less than the thermodynamic equilibrium potential for Li plating, Li deposition will occur unless there is an overpotential associated with the Li deposition reaction. Note that for these experiments, the electrodes were subjected to formation cycling prior to the potentiostatic hold so that the metal coatings were fully reduced and did not contribute additional electron consumption to the measured current. Current profiles reveal that under each potentiostatic condition, the Cu-graphite and Ni-graphite electrodes deliver less lithium-metal plating capacity compared to the uncoated graphite electrode, providing evidence that the metal coatings

do indeed reduce lithium plating. The normalized Li-plating capacities for the metal-coated electrodes were 30-40% lower than the uncoated graphite plating capacity at each voltage hold (Figure 8, Table S7). Post-testing, the electrodes were recovered under an inert atmosphere and X-ray diffraction of the Li-metal (110) peak was measured to quantify the crystalline Li plated on each electrode type. X-ray diffraction is a standard technique for quantification of crystalline materials and is based on the principle that the intensity of the collected pattern is proportional to the concentration of the phase that produces it. 67,68 This method has been used previously to quantify deposited Li in a recent report. 69 The Limetal (110) peak areas normalized against Cu(220) current collector peak areas for the Cu- or Ni-coated electrodes are approximately 50% of the control graphite electrode at each condition (Figure 8, Table S8), validating the electrochemical results. The electrochemical and XRD analyses clearly demonstrate that the metal-coated electrodes reduce Li deposition when the graphite electrode voltage is lower than the thermodynamic equilibrium potential for Li plating, thus providing considerable evidence that the metal films increase the overpotential for the Li deposition reaction.

SEM backscatter images of the electrodes were collected after plating at the 6 h, -20 mV condition (Figure 7g,i). Graphite particles as well as Cu and Ni coatings appear brighter in the images compared with the plated Li due to higher atomic number. On the uncoated graphite electrodes, interconnected dense Li films were observed, covering much of the electrode surface. In contrast, the structure of the graphite electrodes is still apparent in the Cu- and Ni-coated electrodes, which further confirms that nanometer thickness films of Cu and Ni significantly inhibit the deposition of Li metal under voltage conditions where plating occurs. Cross-section SEM images of the electrodes (Figure S17) reveal that the plated Li is contained to the upper layers of the graphite electrode, in good agreement with previous theoretical ^{14,15} and experimental reports. 16,17 In the case of the uncoated graphite electrode, where the quantity of the deposited Li is higher, it is observed that the plated Li extends down into the electrode by approximately 10 nm, reaching the second layer of graphite particles. 16,17 Additional SEM characterization of the Li deposits is presented in the supporting information for both 1000× (Figure S18) and 5000× magnifications (Figure S19). On all three electrode types, similar morphology of the Li deposits is observed. Inspection at 5000× magnification (Figure S19) reveals that the Li deposit morphology consists mainly of irregular, globular-shaped features interdispersed with few higher aspect ratio deposits.

4. CONCLUSIONS

In summary, we demonstrate that Li-metal deposition on graphite electrodes can be suppressed through the increase of the deposition overpotential by modifying the electrode interface with nanoscale coatings of Cu and Ni. XPS results reveal similar species on the surfaces of the uncoated and metal-coated anodes after electrochemical cycling, indicating the minimal impact of metal films on the surface chemistry of the solid electrolyte interphase (SEI). Li-plating experiments demonstrate that the metal films reduce the quantity of the plated Li metal by ~50% compared to uncoated graphite. The efficacy of the metal films, specifically for Ni-coated graphite negative electrodes, as a modification technique to reduce Liplating is apparent at high charge rates. NMC622/Ni-coated graphite pouch cells tested under extreme fast charging conditions (10 min charge time) exhibit enhanced capacity retention with over 90% retention after 300 cycles, corresponding to an ~5% increase compared to cells containing unmodified graphite electrodes. The findings establish that with the rational design of an electrode interface, the overpotential for Li deposition can be modulated, providing a conceptual approach for reducing Li plating on graphite anodes.

ASSOCIATED CONTENT

S Supporting Information

The Supporting Information is available free of charge at https://pubs.acs.org/doi/10.1021/acsami.9b16794.

Experimental details, characterization of graphite and metal-coated electrodes, additional XPS analyses, cell impedance and cycling results, SEM characterization of the plated Li (PDF)

AUTHOR INFORMATION

Corresponding Authors

*E-mail: dbock@bnl.gov (D.C.B.).

*E-mail: esther.takeuchi@stonybrook.edu (E.S.T.).

ORCID ®

Lei Wang: 0000-0002-6348-8344

Amy C. Marschilok: 0000-0001-9174-0474 Kenneth J. Takeuchi: 0000-0001-8129-444X David C. Bock: 0000-0002-2387-7791 Esther S. Takeuchi: 0000-0001-8518-1047

The authors declare no competing financial interest.

ACKNOWLEDGMENTS

This work was supported by the U.S. Department of Energy Office of Energy Efficiency and Renewable Energy under the Advanced Battery Materials Research program, award DE-EE0007785. Method development and in situ and operando cell design was supported by the Center for Mesoscale Transport Properties, an Energy Frontier Research Center supported by the DOE-BES, under award #DE-SC0012673. This research used resources of beamline 5-ID, submicron resolution X-ray spectroscopy (SRX) of the National Synchrotron Light Source II, a U.S. Department of Energy (DOE) Office of Science User Facility operated for the DOE Office of Science by Brookhaven National Laboratory under Contract no. DE-SC0012704. Additionally, this research used resources of the Center for Functional Nanomaterials, which is a U.S. DOE Office of Science Facility, at Brookhaven National Laboratory under Contract no. DE-SC0012704. The authors acknowledge Dr. Ming Lu at the Center for Functional Nanomaterials at Brookhaven National Laboratory for his assistance with DC magnetron sputtering depositions. K.T. acknowledges support from the Science Undergraduate Laboratory Internship (SULI) Program, Brookhaven National Laboratory. E.S.T. acknowledges the William and Jane Knapp Chair for Energy and the Environment.

REFERENCES

- (1) Ahmed, S.; Bloom, I.; Jansen, A. N.; Tanim, T.; Dufek, E. J.; Pesaran, A.; Burnham, A.; Carlson, R. B.; Dias, F.; Hardy, K.; Keyser, M.; Kreuzer, C.; Markel, A.; Meintz, A.; Michelbacher, C.; Mohanpurkar, M.; Nelson, P. A.; Robertson, D. C.; Scoffield, D.; Shirk, M.; Stephens, T.; Vijayagopal, R.; Zhang, J. Enabling Fast Charging - a Battery Technology Gap Assessment. J. Power Sources 2017, 367, 250-262.
- (2) Liu, Q.; Du, C.; Shen, B.; Zuo, P.; Cheng, X.; Ma, Y.; Yin, G.; Gao, Y. Understanding Undesirable Anode Lithium Plating Issues in Lithium-Ion Batteries. RSC Adv. 2016, 6, 88683-88700.
- (3) Tanim, T. R.; Dufek, E. J.; Evans, M.; Dickerson, C.; Jansen, A. N.; Polzin, B. J.; Dunlop, A. R.; Trask, S. E.; Jackman, R.; Bloom, I.; Yang, Z.; Lee, E. Extreme Fast Charge Challenges for Lithium-Ion Battery: Variability and Positive Electrode Issues. J. Electrochem. Soc. 2019, 166, A1926-A1938.
- (4) Lucht, B. L.; Guyomard, D.; Edström, K.; Kostecki, R. Electrochemical Interfaces in Electrochemical Energy Storage Systems. J. Electrochem. Soc. 2015, 162, No. Y13.
- (5) Tikekar, M. D.; Choudhury, S.; Tu, Z.; Archer, L. A. Design Principles for Electrolytes and Interfaces for Stable Lithium-Metal Batteries. Nat. Energy 2016, 1, No. 16114.
- (6) Legrand, N.; Knosp, B.; Desprez, P.; Lapicque, F.; Raël, S. Physical Characterization of the Charging Process of a Li-Ion Battery and Prediction of Li Plating by Electrochemical Modelling. J. Power Sources 2014, 245, 208-216.
- (7) Chandrasekaran, R. Quantification of Bottlenecks to Fast Charging of Lithium-Ion-Insertion Cells for Electric Vehicles. J. Power Sources 2014, 271, 622-632.

- (8) Liu, Q. Q.; Petibon, R.; Du, C. Y.; Dahn, J. R. Effects of Electrolyte Additives and Solvents on Unwanted Lithium Plating in Lithium-Ion Cells. *J. Electrochem. Soc.* **2017**, *164*, A1173—A1183.
- (9) Jurng, S.; Park, S.; Yoon, T.; Kim, H.-s.; Jeong, H.; Ryu, J. H.; Kim, J. J.; Oh, S. M. Low-Temperature Performance Improvement of Graphite Electrode by Allyl Sulfide Additive and Its Film-Forming Mechanism. *J. Electrochem. Soc.* **2016**, *163*, A1798—A1804.
- (10) Park, J.-S.; Lee, M.-H.; Jeon, I.-Y.; Park, H.-S.; Baek, J.-B.; Song, H.-K. Edge-Exfoliated Graphites for Facile Kinetics of Delithiation. *ACS Nano* **2012**, *6*, 10770–10775.
- (11) Bruce, P. G.; Scrosati, B.; Tarascon, J.-M. Nanomaterials for Rechargeable Lithium Batteries. *Angew. Chem., Int. Ed.* **2008**, 47, 2930–2946.
- (12) Cheng, Q.; Yuge, R.; Nakahara, K.; Tamura, N.; Miyamoto, S. KOH Etched Graphite for Fast Chargeable Lithium-Ion Batteries. *J. Power Sources* **2015**, 284, 258–263.
- (13) Kim, T.-H.; Jeon, E. K.; Ko, Y.; Jang, B. Y.; Kim, B.-S.; Song, H.-K. Enlarging the D-Spacing of Graphite and Polarizing Its Surface Charge for Driving Lithium Ions Fast. *J. Mater. Chem. A* **2014**, 2, 7600–7605.
- (14) Arora, P.; Doyle, M.; White, R. E. Mathematical Modeling of the Lithium Deposition Overcharge Reaction in Lithium-Ion Batteries Using Carbon-Based Negative Electrodes. *J. Electrochem. Soc.* **1999**, 146, 3543–3553.
- (15) Hein, S.; Latz, A. Influence of Local Lithium Metal Deposition in 3D Microstructures on Local and Global Behavior of Lithium-Ion Batteries. *Electrochim. Acta* **2016**, 201, 354–365.
- (16) Ghanbari, N.; Waldmann, T.; Kasper, M.; Axmann, P.; Wohlfahrt-Mehrens, M. Detection of Li Deposition by Glow Discharge Optical Emission Spectroscopy in Post-Mortem Analysis. ECS Electrochem. Lett. 2015, 4, A100—A102.
- (17) Ghanbari, N.; Waldmann, T.; Kasper, M.; Axmann, P.; Wohlfahrt-Mehrens, M. Inhomogeneous Degradation of Graphite Anodes in Li-Ion Cells: A Postmortem Study Using Glow Discharge Optical Emission Spectroscopy (GD-OES). J. Phys. Chem. C 2016, 120, 22225–22234.
- (18) Winand, R. Electrocrystallization: Fundamental Considerations and Application to High Current Density Continuous Steel Sheet Plating. *J. Appl. Electrochem.* **1991**, *21*, 377–385.
- (19) Pei, A.; Zheng, G.; Shi, F.; Li, Y.; Cui, Y. Nanoscale Nucleation and Growth of Electrodeposited Lithium Metal. *Nano Lett.* **2017**, *17*, 1132–1139.
- (20) Sagane, F.; Ikeda, K.-i.; Okita, K.; Sano, H.; Sakaebe, H.; Iriyama, Y. Effects of Current Densities on the Lithium Plating Morphology at a Lithium Phosphorus Oxynitride Glass Electrolyte/Copper Thin Film Interface. *J. Power Sources* **2013**, 233, 34–42.
- (21) Zhang, R.; Chen, X.-R.; Chen, X.; Cheng, X.-B.; Zhang, X.-Q.; Yan, C.; Zhang, Q. Lithiophilic Sites in Doped Graphene Guide Uniform Lithium Nucleation for Dendrite-Free Lithium Metal Anodes. *Angew. Chem., Int. Ed.* **2017**, *56*, 7764–7768.
- (22) Yan, K.; Lu, Z.; Lee, H.-W.; Xiong, F.; Hsu, P.-C.; Li, Y.; Zhao, J.; Chu, S.; Cui, Y. Selective Deposition and Stable Encapsulation of Lithium through Heterogeneous Seeded Growth. *Nat. Energy* **2016**, *1*, 1–8.
- (23) Berliner, R.; Fajen, O.; Smith, H. G.; Hitterman, R. L. Neutron Powder-Diffraction Studies of Lithium, Sodium, and Potassium Metal. *Phys. Rev. B: Condens. Matter Mater. Phys.* **1989**, 40, 12086–12097.
- (24) Borders, J. A.; Poate, J. M. Lattice-Site Location of Ion-Implanted Impurities in Copper and Other FCC Metals. *Phys. Rev. B: Condens. Matter Mater. Phys.* **1976**, 13, 969–979.
- (25) Davey, W. P. Precision Measurements of the Lattice Constants of Twelve Common Metals. *Phys. Rev.* **1925**, 25, 753–761.
- (26) Massalski, T. B.; Okamoto, H.; Subramanian, P. R.; Kacprzak, L. *Binary Alloy Phase Diagrams*, 2nd ed.; ASM International: Materials Park, OH, 1990.
- (27) Speranza, G.; Laidani, N. Measurement of the Relative Abundance of sp2 and sp3 Hybridised Atoms in Carbon Based Materials by XPS: A Critical Approach. Part I. *Diamond Relat. Mater.* **2004**, *13*, 445–450.

- (28) Pantea, D.; Darmstadt, H.; Kaliaguine, S.; Roy, C. Electrical Conductivity of Conductive Carbon Blacks: Influence of Surface Chemistry and Topology. *Appl. Surf. Sci.* **2003**, *217*, 181–193.
- (29) Verma, P.; Maire, P.; Novák, P. A Review of the Features and Analyses of the Solid Electrolyte Interphase in Li-Ion Batteries. *Electrochim. Acta* **2010**, 55, 6332–6341.
- (30) Li, L.; Yan, H.; Xu, W.; Yu, D. T.; Heroux, A.; Lee, W. K.; Campbell, S. I.; Chu, Y. S. Pyxrf: Python-Based X-Ray Fluorescence Analysis Package. In X-Ray Nanoimaging: Instruments and Methods I. I. I.; Lai, B.; Somogyi, A., Eds., 2017.
- (31) Ravel, B.; Newville, M. Athena, Artemis, Hephaestus: Data Analysis for X-Ray Absorption Spectroscopy Using Ifeffit. *J. Synchrotron Radiat.* **2005**, *12*, 537–541.
- (32) Mancini, M.; Nobili, F.; Dsoke, S.; D'Amico, F.; Tossici, R.; Croce, F.; Marassi, R. Lithium Intercalation and Interfacial Kinetics of Composite Anodes Formed by Oxidized Graphite and Copper. *J. Power Sources* **2009**, *190*, 141–148.
- (33) Nobili, F.; Dsoke, S.; Mancini, M.; Tossici, R.; Marassi, R. Electrochemical Investigation of Polarization Phenomena and Intercalation Kinetics of Oxidized Graphite Electrodes Coated with Evaporated Metal Layers. *J. Power Sources* **2008**, *180*, 845–851.
- (34) Suzuki, J.; Yoshida, M.; Nakahara, C.; Sekine, K.; Kikuchi, M.; Takamura, T. Li Mass Transfer through a Metallic Copper Film on a Carbon Fiber During the Electrochemical Insertion/Extraction Reaction. *Electrochem. Solid-State Lett.* **2001**, *4*, A1–A4.
- (35) Nobili, F.; Dsoke, S.; Mancini, M.; Marassi, R. Interfacial Properties of Copper-Coated Graphite Electrodes: Coating Thickness Dependence. *Fuel Cells* **2009**, *9*, 264–268.
- (36) Evmenenko, G.; Fister, T. T.; Buchholz, D. B.; Castro, F. C.; Li, Q.; Wu, J.; Dravid, V. P.; Fenter, P.; Bedzyk, M. J. Lithiation of Multilayer Ni/NiO Electrodes: Criticality of Nickel Layer Thicknesses on Conversion Reaction Kinetics. *Phys. Chem. Chem. Phys.* **2017**, *19*, 20029–20039.
- (37) Chen, H.; Ling, M.; Hencz, L.; Ling, H. Y.; Li, G.; Lin, Z.; Liu, G.; Zhang, S. Exploring Chemical, Mechanical, and Electrical Functionalities of Binders for Advanced Energy-Storage Devices. *Chem. Rev.* **2018**, *118*, 8936–8982.
- (38) Biesinger, M. C. Advanced Analysis of Copper X-Ray Photoelectron Spectra. Surf. Interface Anal. 2017, 49, 1325–1334.
- (39) Wu, C.-K.; Yin, M.; O'Brien, S.; Koberstein, J. T. Quantitative Analysis of Copper Oxide Nanoparticle Composition and Structure by X-Ray Photoelectron Spectroscopy. *Chem. Mater.* **2006**, *18*, 6054–6058.
- (40) Biesinger, M. C.; Payne, B. P.; Lau, L. W. M.; Gerson, A.; Smart, R. S. C. X-Ray Photoelectron Spectroscopic Chemical State Quantification of Mixed Nickel Metal, Oxide and Hydroxide Systems. *Surf. Interface Anal.* **2009**, *41*, 324–332.
- (41) Grosvenor, A. P.; Biesinger, M. C.; Smart, R. S. C.; McIntyre, N. S. New Interpretations of XPS Spectra of Nickel Metal and Oxides. *Surf. Sci.* **2006**, *600*, 1771–1779.
- (42) Chen, K.; Song, S.; Xue, D. Faceted Cu2o Structures with Enhanced Li-Ion Battery Anode Performances. *CrystEngComm* **2015**, 17, 2110–2117.
- (43) Li, Q.; Huang, G.; Yin, D.; Wu, Y.; Wang, L. Synthesis of Porous Nio Nanorods as High-Performance Anode Materials for Lithium-Ion Batteries. *Part. Part. Syst. Charact.* **2016**, 33, 764–770.
- (44) An, S. J.; Li, J.; Daniel, C.; Mohanty, D.; Nagpure, S.; Wood, D. L. The State of Understanding of the Lithium-Ion-Battery Graphite Solid Electrolyte Interphase (SEI) and Its Relationship to Formation Cycling. *Carbon* **2016**, *105*, 52–76.
- (45) Benitez, L.; Seminario, J. M. Ion Diffusivity through the Solid Electrolyte Interphase in Lithium-Ion Batteries. *J. Electrochem. Soc.* **2017**, *164*, E3159—E3170.
- (46) Liu, C.; Li, C.; Ahmed, K.; Mutlu, Z.; Ozkan, C. S.; Ozkan, M. Template Free and Binderless NiO Nanowire Foam for Li-Ion Battery Anodes with Long Cycle Life and Ultrahigh Rate Capability. *Sci. Rep.* **2016**, *6*, No. 29183.

- (47) Wang, X.; Li, X.; Sun, X.; Li, F.; Liu, Q.; Wang, Q.; He, D. Nanostructured NiO Electrode for High Rate Li-Ion Batteries. *J. Mater. Chem.* **2011**, *21*, 3571–3573.
- (48) Shi, L.; Fan, C.; Sun, C.; Ren, Z.; Fu, X.; Qian, G.; Wang, Z. Synthesis of Different Cuo Nanostructures from Cu(OH)₂ Nanorods through Changing Drying Medium for Lithium-Ion Battery Anodes. RSC Adv. 2015, 5, 28611–28618.
- (49) Peled, E.; Menkin, S. Review—SEI: Past, Present and Future. J. Electrochem. Soc. 2017, 164, A1703—A1719.
- (50) Yamaki, J.-I.; Tobishima, S.-I.; Hayashi, K.; Keiichi, S.; Nemoto, Y.; Arakawa, M. A Consideration of the Morphology of Electrochemically Deposited Lithium in an Organic Electrolyte. *J. Power Sources* 1998, 74, 219–227.
- (51) Petzl, M.; Danzer, M. A. Nondestructive Detection, Characterization, and Quantification of Lithium Plating in Commercial Lithium-Ion Batteries. *J. Power Sources* **2014**, *254*, 80–87.
- (52) Peled, E. The Electrochemical Behavior of Alkali and Alkaline Earth Metals in Nonaqueous Battery Systems—the Solid Electrolyte Interphase Model. *J. Electrochem. Soc.* **1979**, *126*, 2047–2051.
- (53) Ellis, L. D.; Allen, J. P.; Hill, I. G.; Dahn, J. R. High-Precision Coulometry Studies of the Impact of Temperature and Time on Sei Formation in Li-Ion Cells. *J. Electrochem. Soc.* **2018**, *165*, A1529–A1536.
- (54) Malmgren, S.; Ciosek, K.; Hahlin, M.; Gustafsson, T.; Gorgoi, M.; Rensmo, H.; Edström, K. Comparing Anode and Cathode Electrode/Electrolyte Interface Composition and Morphology Using Soft and Hard X-Ray Photoelectron Spectroscopy. *Electrochim. Acta* **2013**, *97*, 23–32.
- (55) Aurbach, D.; Markovsky, B.; Weissman, I.; Levi, E.; Ein-Eli, Y. On the Correlation between Surface Chemistry and Performance of Graphite Negative Electrodes for Li Ion Batteries. *Electrochim. Acta* 1999, 45, 67–86.
- (56) Lesiak, B.; Jablonski, A.; Prussak, Z.; Mrozek, P. Experimental Determination of the Inelastic Mean Free Path of Electrons in Solids. *Surf. Sci.* **1989**, 223, 213–232.
- (57) Tanuma, S.; Powell, C. J.; Penn, D. R. Calculations of Electron Inelastic Mean Free Paths. Ix. Data for 41 Elemental Solids over the 50 eV to 30 KeV Range. *Surf. Interface Anal.* **2011**, 43, 689–713.
- (58) Tanuma, S.; Powell, C. J.; Penn, D. R. Calculations of Electorn Inelastic Mean Free Paths. II. Data for 27 Elements over the 50–2000 eV Range. *Surf. Interface Anal.* **1991**, *17*, 911–926.
- (59) Bock, D. C.; Waller, G. H.; Mansour, A. N.; Marschilok, A. C.; Takeuchi, K. J.; Takeuchi, E. S. Investigation of Solid Electrolyte Interphase Layer Formation and Electrochemical Reversibility of Magnetite, Fe₃O₄, Electrodes: A Combined X-Ray Absorption Spectroscopy and X-Ray Photoelectron Spectroscopy Study. *J. Phys. Chem. C* 2018, 122, 14257–14271.
- (60) Dedryvère, R.; Martinez, H.; Leroy, S.; Lemordant, D.; Bonhomme, F.; Biensan, P.; Gonbeau, D. Surface Film Formation on Electrodes in a LiCoO₂/Graphite Cell: A Step by Step XPS Study. *J. Power Sources* **2007**, *174*, 462–468.
- (61) Leroy, S.; Blanchard, F.; Dedryvère, R.; Martinez, H.; Carré, B.; Lemordant, D.; Gonbeau, D. Surface Film Formation on a Graphite Electrode in Li-Ion Batteries: AFM and XPS Study. Surf. Interface Anal. 2005, 37, 773–781.
- (62) Lu, W.; Xiong, S.; Xie, K.; Pan, Y.; Zheng, C. Identification of Solid Electrolyte Interphase Formed on Graphite Electrode Cycled in Trifluoroethyl Aliphatic Carboxylate-Based Electrolytes for Low-Temperature Lithium-Ion Batteries. *Ionics* **2016**, *22*, 2095–2102.
- (63) Niehoff, P.; Passerini, S.; Winter, M. Interface Investigations of a Commercial Lithium Ion Battery Graphite Anode Material by Sputter Depth Profile X-Ray Photoelectron Spectroscopy. *Langmuir* **2013**, 29, 5806–5816.
- (64) Randles, J. E. B. Kinetics of Rapid Electrode Reactions. *Discuss. Faraday Soc.* 1947, 1, 11–19.
- (65) Sethuraman, V. A.; Kowolik, K.; Srinivasan, V. Increased Cycling Efficiency and Rate Capability of Copper-Coated Silicon Anodes in Lithium-Ion Batteries. *J. Power Sources* **2011**, *196*, 393–398.

- (66) Yu, P.; Ritter, J. A.; White, R. E.; Popov, B. N. Ni-Composite Microencapsulated Graphite as the Negative Electrode in Lithium-Ion Batteries. II. Electrochemical Impedance and Self-Discharge Studies. *J. Electrochem. Soc.* **2000**, *147*, 2081–2085.
- (67) Copeland, L. E.; Bragg, R. H. Quantitative X-Ray Diffraction Analysis. *Anal. Chem.* **1958**, *30*, 196–201.
- (68) Klug, H. P.; Alexander, L. E. X-Ray Diffraction Procedures: For Polycrystalline and Amorphous Materials; John Wiley & Sons, 1974.
- (69) Zheng, J.; Tang, T.; Zhao, Q.; Liu, X.; Deng, Y.; Archer, L. A. Physical Orphaning Versus Chemical Instability: Is Dendritic Electrodeposition of Li Fatal? ACS Energy Lett. 2019, 4, 1349–1355.